VIP *Very Important Paper*

Not Just Another Methanation Catalyst: Depleted Uranium Meets Nickel for a High-Performing Process Under Autothermal Regime

Lai Truong-Phuoc,*[a] Jean-Mario Nhut,[a] Secou Sall,[a] Giulia Tuci,[b] Andrea Rossin,[b] Vasiliki Papaefthimiou,[a] Cuong Duong-Viet,[a] Corinne Petit,[a] Mehdi Arab,[c] Alex Jourdan,[c] Loic Vidal,[d] Giuliano Giambastiani,*[a, b] and Cuong Pham-Huu*[a]

Ni-based catalysts prepared through impregnation of depleted uranium oxides (DU) have successfully been employed as highly efficient, selective, and durable systems for CO_2 hydrogenation to substituted natural gas (SNG; CH_4) under an autothermal regime. The thermo-physical properties of DU and the unique electronic structure of f-block metal-oxides combined with a nickel active phase, generated an ideal catalytic assembly for turning waste energy back into useful energy for catalysis. In particular, Ni/UO_x stood out for the capacity of DU matrix to control the extra heat (hot-spots) generated at its surface by the highly exothermic methanation process. At odds with the benchmark $Ni/\gamma\text{-}Al_2O_3$ catalyst, the double action played by DU as a "thermal mass" and "dopant" for the nickel active phase

unveiled the unique performance of Ni/UO_x composites as CO_2 methanation catalysts. The ability of the weakly radioactive ceramic (UO_x) to harvest waste heat for more useful purposes was demonstrated in practice within a rare example of a highly effective and long-term methanation operated under autothermal regime (i.e., without any external heating source). This finding is an unprecedented example that allows a real step-forward in the intensification of "low-temperature" methanation with an effective reduction of energy wastes. At the same time, the proposed catalytic technology can be regarded as an original approach to recycle and bring to a second life a less-severe nuclear by-product (DU), providing a valuable alternative to its more costly long-term storage or controlled disposal.

Introduction

The growth of renewable energy capacity from carbon-neutral sources (i.e., solar, wind) is limited by the intermittent nature of the renewable flow as well as from the lack of adequate and cost-effective solutions for the short- and long-term energy storage. Water electrolysis to oxygen (O_2) and green hydrogen

[a] Dr. L. Truong-Phuoc, Dr. J.-M. Nhut, Dr. S. Sall, Dr. V. Papaefthimiou, Dr. C. Duong-Viet, Prof. C. Petit, Dr. G. Giambastiani, Dr. C. Pham-Huu
Institute of Chemistry and Processes for Energy, Environment and Health (ICPEES), ECPM
UMR 7515 of the CNRS and University of Strasbourg
25 rue Becquerel, 67087 Strasbourg Cedex 02 (France)
E-mail: ltruong-phuoc@blackleaf.fr
cuong.pham-huu@unistra.fr
giuliano.giambastiani@iccom.cnr.it
[b] Dr. G. Tuci, Dr. A. Rossin, Dr. G. Giambastiani
Institute of Chemistry of OrganoMetallic Compounds
ICCOM-CNR and Consorzio INSTM
Via Madonna del Piano, 10, 50019 Sesto F.no, Florence (Italy)
[c] Dr. M. Arab, Dr. A. Jourdan
ORANO Tricastin, Direction de La Recherche & Développement, Site du TRICASTIN BP 16
26701 Pierrelatte Cedex (France)
[d] Dr. L. Vidal
The Mulhouse Materials Science Institute (IS2 M)
15, rue Jean Starcky - BP 2488, 68057 Mulhouse cedex (France)

Supporting information for this article is available on the WWW under https://doi.org/10.1002/cssc.202201859

(H$_2$) as fuel is a technology at hand for the electrical-to-chemical energy storage.[1] However, higher-density fuels (e.g., CH_4 or higher hydrocarbons) remain preferred targets in the power-to-gas (P2G) technology. Indeed, the lack of hydrogen pipeline networks to connect H_2 producers with end-users still limits the transition to a mature hydrogen-based economy. Among carbon capture and utilization (CCU) technologies, methanation reaction [i.e., the reaction of H_2 with CO_2 to give methane substitute natural gas (SNG)][2] is gaining importance in the contemporary industrial society. This reaction offers a solution to the use of green hydrogen into sustainable decarbonization strategies where CO_2 or biogas (25–50% of CO_2) derived from methanization of biomasses[3] is converted into SNG as a fuel to be distributed through the existing gas grids. Methanation allows carbon to be moved through industrial systems without any net removal of CO_2 from the atmosphere,[4,5] but with zero net emissions of new greenhouse gases (GHGs) by displacing the use of fossil fuels.[6]

As humans intensify their search for zero-GHG-emission energy sources, the demand for enriched uranium as a fissile nuclear fuel is expected to increase in the years to come.[7] The limitations encountered in obtaining significant quantities of this toxic and radioactive element (together with its potential negative impact on health and environment) discourage its use for purposes other than that of fuel in nuclear reactors. In contrast, programs for ^{235}U fissile isotope enrichment offer researchers several opportunities for a practical and beneficial use of the weakly radioactive ^{238}U (alpha emitter) as the principal constituent of the more stable depleted uranium (DU).

The concentration of the fissile isotope ^{235}U passes from 0.72% in the natural composition to 0.3–0.2% in the depleted form (DU). Accordingly, the latter holds an isotopic composition dominated by the less radioactive and non-fissile ^{238}U at 99.97% along with percentages of ^{235}U and ^{234}U of around 0.2 and 0.000898%, respectively. Its composition consists in a mixture of metal-oxides where uranium appears in its most common oxidation states +4 (UO_2), +5 and +6 (U_3O_8),[8] and +6 (UO_3).[9]

The Word Information Service on Energy (WISE) through the uranium project has estimated over 1 million tons of DU in stock worldwide since the end of the last century.[10] At odds with restrictions typically encountered in obtaining and managing significant amounts of this ceramic (due to a persistent toxicity associated to the perception of negative health and environmental impact), some time ago the U.S. Department of Energy has started an investigation plan dealing with the fundamental chemistry of DU.[11] Their aim was to determine the beneficial usefulness of stored DU in a variety of catalytic applications. Accordingly, new classes of catalysts containing DU as the active component were investigated and successfully employed for the decomposition of organic volatiles (VOCs), including alkanes and aromatics with environmental remediation purposes.[12] Two relatively recent Reviews by Ismagilov et al.[13,14] offer an exhaustive overview on the use of DU as either active phase or support in mixed metal-based materials for catalysis. Recent years have also witnessed a steadily growing interest in early actinide elements, uranium included, in the preparation of discrete organometallic compounds with unique and distinctive properties with respect to more conventional transition-metal- and lanthanide-based complexes for catalysis.[15–20] As far as DU is concerned, its unique physical properties have contributed to mark important differences between this ceramic and other more conventional oxides, classically employed in catalysis. This weakly radioactive oxide[21,22] possesses a non-porous/macroporous nature that translates into samples with a generally very-low specific surface area (see below). On the other hand, it has a very high density (19.3 g cm^{-3}) that is about 41% higher than that of lead and hence much higher of that of common and commercially available metal oxides employed in heterogeneous catalysis (Table 1).

Table 1 lists all the main thermo-physical properties of the most representative oxide-based ceramics classically employed in industrially relevant heterogeneous processes at comparison

with DU. Besides its highest density, DU also exhibits the lowest specific thermal capacity (C_p) in a relatively wide range of temperatures and the lowest thermal conductivity (κ). Both features confer DU unique and distinctive properties with respect to classical p-, d-, or f-block counterparts in the list.[31]

Herein, we demonstrate the use of DU as a non-innocent carrier for the preparation of nickel-based composites at variable d-metal loading as highly efficient, durable, and selective catalysts for the CO_2-to-SNG conversion under exceptionally low reaction temperatures (external heat) or even under an autothermal methanation regime (external heater switched off). Previous reports have already claimed the use of DU in combination with Ni nanoparticles (NPs) for CO_2 methanation,[32–35] although key and distinctive features of this catalyst technology have not been unveiled yet. Irrespective to the adiabatic nature of the reactor setup, we have demonstrated that Ni/UO_x composites realize an ideal catalytic assembly for operating the catalytic process under an autothermal regime. Indeed, the extra heat produced by the exothermic process is harvested and exploited in turn as a useful energy source to keep the methanation reaction alive even when its primary external heating source is switched off.[36] Besides the outstanding methanation performance obtained with Ni/UO_x catalysts under exceptionally low temperature settings, the study offers a concrete solution to the challenging problem of the extra heat harvesting looking beyond the simple employment of adiabatic reactor schemes.[37] Ni/UO_x catalysts have also shown remarkable stability and durability throughout a very long-term methanation run (> 400 h). Evidence for a permanent catalyst modification with the generation of Ni/UO_x core–shell-like composites (as the result of an extensive segregation of UO_x particles all around larger Ni NPs aggregates) is also provided and discussed.

Results and Discussion

Synthesis and characterization of $^kNi/R$ catalysts

Nickel phase deposition in $^kNi/R$ (1–5) catalysts (1 and 3: k = 10 wt%; 2 and 4: 20 wt%; 5: 2 wt%; 1, 2, and 5: R=UO_x; 3 and 4: R = γ-Al_2O_3) was obtained by wet impregnation (WI) technique followed by conventional thermal calcination/reduction steps (see the Experimental Section for details).[38] All composites

Table 1. Thermo-physical properties of various ceramics classically employed as carriers in heterogeneous catalysis at comparison with DU (UO_x).

Metal oxide	Specific thermal capacity [J kg^{-1} K^{-1}]	Density [g cm^{-3}]	Thermal conductivity [W mK^{-1}]
DU (UO_x)	119 (373 K)[23] 167 (773 K)[23]	19.07[24]–19.3[25]	0.431 (773 K)[23]
γ-Al_2O_3	1048 (298 K)[26]	3.98[27]	25.104 (298 K)[27] 14.64 (773 K)[27]
CeO_2	386 (373 K)[28]	7.28[27]	9.58 (673 K)[27]
TiO_2	682 (298 K)[29]	4.25[27]	6.69 (373 K)[27] 3.77 (673 K)[27]
ZrO_2	489 (298 K)[30]	5.56[27]	2.09 (373 K)[27] 2.09 (673 K)[27]

ChemSusChem

Research Article
doi.org/10.1002/cssc.202201859

Chemistry Europe
European Chemical
Societies Publishing

were thoroughly characterized through powder X-ray diffraction (PXRD), transmission electron microscopy (TEM), scanning transmission electron microscopy (STEM), selected-area electron diffraction (SAED), N_2-physisorption, and H_2-chemisorption analyses while their effective metal loading was determined (on NiO pre-catalysts) by inductively coupled plasma atomic emission spectroscopy (ICP-AES) measurements. Table 2 outlines all samples of the present study along with their effective nickel charge.

All composites from this series were firstly analyzed through PXRD. This analysis was carried out to check the reduction extent of the NiO particles during their conversion into catalysts **1–5** and to give (whenever possible) a first assessment on the average size of Ni NPs formed. Regrettably, only high- or medium-nickel-loaded samples (**2** and **4**) gave useful information on the oxidation state and average size of nickel particles. Figure 1A shows the PXRD patterns of plain DU beads along with those of pre-catalyst ^{20}NiO/UO$_x$ and its reduced counterpart ^{20}Ni/UO$_x$ (**2**).

The analysis of DU in samples **1** and **2** exhibits complex systems containing mixtures of UO$_x$ at variable metal oxidation state [uranium dioxide (UO$_2$), α-triuranium octoxide (U$_3$O$_8$), and γ-uranium trioxide (UO$_3$)], whose relative ratio depends on the chemical treatments these samples underwent. U$_3$O$_8$ is defi-

nitely the most abundant and stable chemical form available in the starting DU as well as the prevalent oxide species obtained upon heating all uranium oxides over 650 °C under an oxidizing atmosphere.

NiO peaks are more evident in the calcined pre-catalysts containing a higher theoretical nickel loading (i.e., 20 wt%). These diffraction signals at $2\theta = 37.2$, 43.2, and 62.9° together with two minor components at 75.2 and 79.4° can be readily indexed as (111), (200), (220), (311), and (222) crystal planes of NiO NPs.[39] The successive sample reduction under a pure stream of H_2 at 350 °C for 2 h to give sample **2** changes the PXRD profile appreciably (Figure 1A, red vs. blue).

Indeed, UO$_2$ is now the prevalent form of DU (Figure 1A, blue line) whereas NiO diffraction peaks are definitively suppressed (at least for those NiO signals not overlapping minor DU oxide components). As the PXRD profile of **2** shows, the relatively well-isolated component at $2\theta = 51.8°$ along with a minor shoulder at $2\theta = 76.4°$ can be indexed as (200) and (220) crystal planes of Ni^0.[40] A rough estimation of Ni NPs sizes was obtained by the application of the Scherrer equation[41] to the peak full width at half maximum (FWHM) of the diffraction component at $2\theta = 44.5°$ (111) (FWHM = 0.74 ± 0.1). The remaining peaks of metallic Ni at $2\theta = 51.8°$ (200) and $2\theta = 76.4°$ (220) are partially overlapped by the reflections of U$_3$O$_8$ and UO$_2$.[42] Accordingly, the estimated mean Ni NPs size in **2** was 12.1 ± 1.8 nm. Similarly, a rough size estimation of Ni NPs on the benchmark Ni/γ-Al$_2$O$_3$ catalysts was possible on the higher metal loaded samples only. Figure 1B illustrates the PXRD pattern of ^{20}Ni/γ-Al$_2$O$_3$ (**4**) together with that of the ^{20}NiO/γ-Al$_2$O$_3$ pre-catalyst and the plain γ-Al$_2$O$_3$ support. As for the latter, it consists in four well-defined components visible in all spectra at $2\theta = 37.5$, 39.2, 45.7, and 66.7° attributed to (311), (222), (400), and (440) crystal planes, respectively.[43] NiO diffraction peaks of the calcined pre-catalyst (red curve in Figure 1B; $2\theta = 37.2$, 43.2, 62.9, 75.2, and 79.4°)[39] are no longer visible in its reduced counterpart (**4**, Figure 1B, blue line). On the other hand, crystal planes (200) and (220) of metallic Ni are readily attributable from the PXRD pattern of **4**. The Scherrer equation applied to the FWHM (0.86 ± 0.1) of the component at $2\theta = 51.8°$ [indexed as the (200) Miller planes of Ni^0] in **4** was consistent with a mean Ni NPs size of 10.7 ± 1.3 nm.

Table 2. ICP-AES analyses on samples **1–5** and **1'**.

Entry	Sample[a,b]	Ni[c] [wt.%]
1	^{10}Ni/UO$_x$ (**1**) fresh	9.91
2[d]	^{10}Ni/UO$_x$ (**1'**) spent	9.58
3	^{20}Ni/UO$_x$ (**2**)	17.52
4	^{10}Ni/γ-Al$_2$O$_3$ (**3**)	8.60
5	^{20}Ni/γ-Al$_2$O$_3$ (**4**)	18.77
6	^{2}Ni/UO$_x$ (**5**)	2.24

[a] Superscripts in the name of samples **1–5** and **1'** refer to their theoretical loading. This is maintained in the name of composites throughout the manuscript. [b] Except for sample **1'** (entry 2), ICP analyses were conducted on the NiO pre-catalysts obtained after the impregnation/calcination steps, and effective nickel loadings were used in the calculation of the process rate λ (see below). [c] Average values calculated over three independent ICP-AES analyses. [d] Catalyst recovered after a long-term methanation run (> 400 h) (see below).
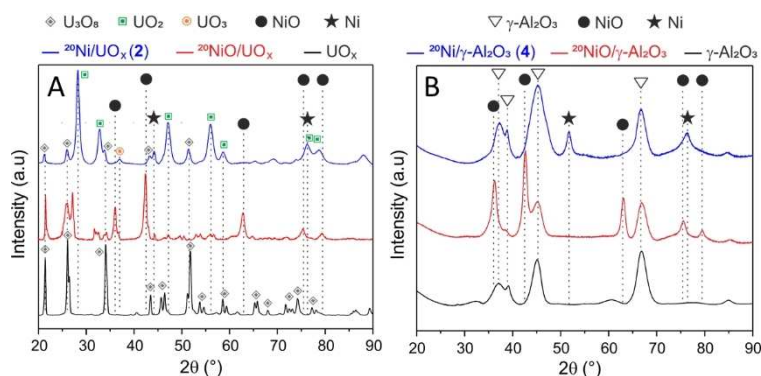
Figure 1. PXRD profiles. (A) UO$_x$ (black curve), ^{20}NiO/UO$_x$ pre-catalyst (red curve), and ^{20}Ni/UO$_x$ (**2**) (blue curve). (B) γ-Al$_2$O$_3$ (black curve), ^{20}NiO/γ-Al$_2$O$_3$ (red curve), and ^{20}Ni/γ-Al$_2$O$_3$ (blue curve) (**4**).

ChemSusChem

Research Article
doi.org/10.1002/cssc.202201859

Chemistry Europe
European Chemical
Societies Publishing

STEM combined with energy-dispersive X-ray spectroscopy (EDS) is used to evaluate the metal active phase dispersion on freshly prepared UO_x- and γ-Al_2O_3-based catalysts, revealing a pretty good and homogeneous distribution of all elements throughout the whole scanned areas (Figure 2 and Figure S2). The low contrast of Ni NPs in UO_x-containing samples (**1**, **2**, and **5**) hampers an accurate determination of the ultimate metal particle size. However, high-resolution (HR)TEM images carried out on **1** have clearly shown the presence of nickel and uranium phases. Interfringe distances of 0.31 and 0.21 nm measured on the sample (Figure 2B) are in line with the presence of (111) lattice planes of UO_2[44] and Ni,[45,46] respectively. SAED pattern recorded on **1** (Figure S2F) has finally confirmed the presence of discontinuous diffraction rings ascribable to (111), (200), (220) and (311) Bragg reflections of a cubic fcc-type UO_2 structure[47] and to (111), (200), and (220) reflections of cubic fcc Ni-NPs.[48] EDS images recorded on the freshly prepared **1** (Figure 2Ca–d) finally exhibit a pretty good and homogeneous elements dispersion on the whole scanned area.

More information on Ni NPs size and distribution were obtained from TEM analysis of the two γ-Al_2O_3-based samples **3** and **4**. Figure S3 (Supporting Information) shows a pretty good dispersion and dense distribution of Ni NPs on both samples with an estimated average particle size of about 10 ± 2 and 14 ± 2 nm for **3** and **4**, respectively, as determined from a statistical analysis over 60–80 particles (see histograms in Figure S3). Table 3 lists all main chemico-physical details recorded on catalysts **1–5** including metal dispersion (D, %) and

Ni exposed surface areas (S_{Ni}, $m^2 g_{Ni}^{-1}$) as determined for each composite by H_2 chemisorption analysis. As far as UO_x-based Ni-catalysts are concerned, metallic surface areas were in good accord with previous literature reports,[49] showing an almost linear relationship between the nominal nickel content and the ultimate surface exposed metallic area. A plain DU oxide sample was also employed for a blank chemisorption test at room temperature. As expected, it did not show any H_2 chemisorption aptitude.[33,49]

Expectedly, D measured on the γ-Al_2O_3-based samples (Table 3, entries 5 and 6) were always higher than those recorded on macroporous and low-surface area UO_x-based catalysts (Table 3, entries 3, 4, and 7). Accordingly, the nickel active surface area measured on the most representative UO_x-based catalyst **1** was more than two times lower than that measured on its benchmark γ-Al_2O_3-based counterpart (**3**) (Table 3, entry 3 vs. 5).

The catalysts' specific surface areas (SSA) along with the respective total pore volume (except for macroporous UO_x-based samples) are listed in Table 3, while N_2 adsorption/desorption isothermal linear plots are outlined in Figure S4 (Supporting Information).

γ-Al_2O_3-based composites (**3** and **4**) exhibit classical Type IV isotherms with moderate but distinctive H4 hysteresis loops in the 0.4–1.0 p/p_0 range, typical of mesoporous structures featured by complex pore networks of ill-defined shape.[50] The higher the nickel loading, the lower the SSA and the pore size in γ-Al_2O_3-based samples.
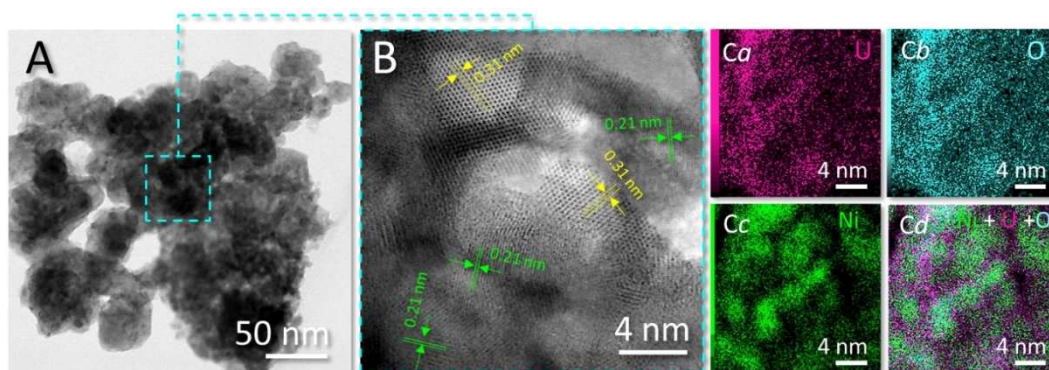

Figure 2. (A,B) TEM images recorded on **1** at different magnifications. (Ca–d) EDS elemental mapping of (B).

Table 3. H_2 chemisorption data for samples **1–5**. BET surface areas and total pore volumes of all composites and their bare UO_x and γ-Al_2O_3 supports.

Entry	Sample	D[a] [%]	S_{Ni}[a] [$m^2 g_{Ni}^{-1}$]	Ni NP size[b] [nm]	SSA[c,d] [$m^2 g^{-1}$]	$V_{p(total)}$[e] [$cm^3 g^{-1}$]
1	UO_x	–	–	–	1[d]	–
2	γ-Al_2O_3	–	–	–	234[c]	0.700
3	^{10}Ni/UO_x (**1**)	4.0	26.6	n.d.	11[d]	–
4	^{20}Ni/UO_x (**2**)	6.3	42.1	12.1 ± 1.8	18[d]	–
5	^{10}Ni/γ-Al_2O_3 (**3**)	14.9	61.2	n.d.	222[c]	0.652
6	^{20}Ni/γ-Al_2O_3 (**4**)	12.8	49.3	10.7 ± 1.3	196[c]	0.551
7	^{2}Ni/UO_x (**5**)	2.7	7.1	n.d.	4[d]	–

[a] Measured by H_2 chemisorption analysis. [b] Mean value estimated by the Scherrer equation on XRD profiles. [c] Brunauer–Emmett–Teller (BET) SSA measured using N_2 at the liquid N_2 temperature (77 K). [d] SSA values measured using Kr at the liquid N_2 temperature (77 K). [e] Total pore volume of micro/mesoporous samples (γ-Al_2O_3, **3** and **4**) determined by the N_2 adsorption branch of isotherms at $p/p_0=0.98$.

ChemSusChem

Research Article
doi.org/10.1002/cssc.202201859

**Chemistry
Europe**
European Chemical
Societies Publishing

An opposite trend was observed for the Ni-catalysts prepared on the less conventional non-porous/macroporous DU whose SSA measured using Kr at the temperature of liquid N_2 (77 K)[51] were found to slightly increase with the ultimate metal loading (Table 3, entry 1 vs.7, 3, and 4).

CO$_2$ methanation with ^{k}Ni/R catalysts: influence of reaction temperature and reagents flow rate

The study was initially carried out on Ni/UO$_x$-based catalysts and benchmarked with classical Ni/γ-Al$_2$O$_3$ counterparts. In a typical methanation trial, 500 mg of each catalyst were packed inside a tubular reactor and pre-treated for 2 h at 350 °C under a pure hydrogen stream (see Experimental Section for details). Temperature values were constantly monitored throughout the whole catalytic runs by a system of three thermocouples located in proximity of the quartz tube reactor (T_F) and inside the catalyst bed (T_C) (see below and Figure S1). Before starting the methanation test, each catalyst was stabilized at the desired target temperature under a pure stream of Ar and maintained at that value till reaching a maximum temperature deviation of approximately ± 3 °C between T_F and T_C (average temperature measured between the two thermocouples). Afterwards, a stream of H$_2$/CO$_2$ (4 v/v) at ambient pressure and temperature was introduced downward through the catalyst bed at a given gas hourly space velocity (GHSV) (10000–30000 mL g^{-1} h^{-1}). Importantly, whichever catalyst was used, the process was monitored throughout a complete forth and back sweeping cycle of the reactor temperature (T_F) in the 170–350 °C range. Figure 3A highlights the performance of catalysts **1** and **3** under identical operational conditions, using 10000 mL g^{-1} h^{-1} as starting GHSV.

The two Ni-catalysts behave differently, with the UO$_x$-based **1** showing net improved catalytic performance compared to that of Ni/γ-Al$_2$O$_3$ (**3**). In particular, **1** exhibits excellent performance already at temperature values much lower than those required by **3** to get comparable process rates (λ). Remarkably, a more rapid process ignition takes place on **1** upon increasing the reactor temperature (T_F). As Figure 3B shows, the average temperature measured at the catalytic bed (T_C) increases suddenly of more than 60 °C upon varying the reactor temperature setting (T_F) between 195 and 205 °C. On the other hand, a more gradual increase of the temperature gap (T_C vs. T_F) is measured with **3** (Figure 3C), with a maximum ΔT when the catalyst approaches its higher productivity ($T_F = 350$ °C, $T_C = 400$ °C; Figure 3C).

The different performance of catalysts nominally sharing the same metal active phase loading (10 wt%) was tentatively ascribed to a synergistic and more favorable interaction between nickel NPs and UO$_x$ in **1**. Such a beneficial interaction was even more relevant while considering the non-porous/macroporous nature of DU and (more generally) its less appealing morphological properties as an active phase carrier when compared with γ-Al$_2$O$_3$ (see Table 3).

To rationalize these outcomes, it is important to remember that among all the main metal oxides classically employed as
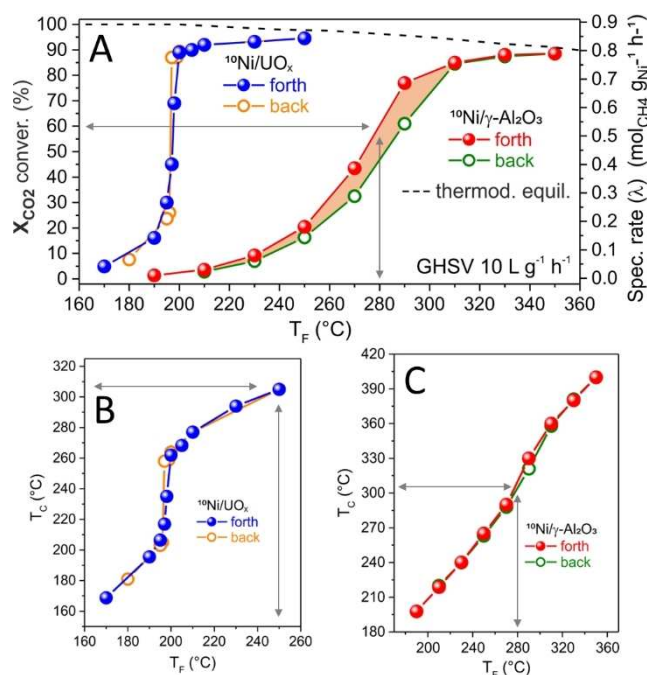
Figure 3. (A) CO$_2$ methanation with ^{10}Ni/R [R = UO$_x$ (**1**) or γ-Al$_2$O$_3$ (**3**)] as a function of the reactor temperature setting (T_F). All catalysts were tested without any thermic diluent using the following reaction conditions: catalyst weight = 500 mg, GHSV (STP) = 10000 mL g^{-1} h^{-1}, [CO$_2$] = 20 vol%, [H$_2$] = 80 vol%, H$_2$/CO$_2$ = 4, total flow rate = 83.3 mL min^{-1}, atmospheric pressure. Full and empty spheres refer to the forth and back temperature scan, respectively. CH$_4$ selectivity (S_{CH_4}, not shown) was constantly 100% in the whole temperature range. S_{CH_4} values are reported in Figure S5 for the sake of completeness. The dashed black line refers to the conversion at the thermodynamic equilibrium. Forth and back methanation profiles of **1** and **3** were recorded within 8–9 h and each temperature value was left to stabilize not less than 30 min before recording the data. (B,C) Variation of the temperature values experimentally recorded at the catalyst bed (T_C) vs. those measured at the furnace walls (T_F).

supports in heterogeneous catalysis, DU oxides feature the highest density, the lowest specific heat capacity (C_p), and the lowest thermal conductivity (κ) at one time (Table 1). The sudden increase of T_C values in a narrow range of reactor temperature settings (ΔT_F; Figure 3B) is certainly linked to the formation of hot-spots generated at the catalyst bed throughout the highly exothermic methanation process. In spite of the pyrophoric nature of DU,[25] the strongly reductive (H$_2$ flow) and anaerobic environment where CO$_2$ methanation occurs led us to exclude any DU self-ignition/oxidation phenomena.[52]

On the other hand, thermo-physical properties of DU allow harvesting the extra heat originated by the methanation exothermicity and turn it back into useful energy (heat) for the process to occur. While the lowest C_p of DU makes easier its temperature increase per mass (by heat exchange with the reaction exothermicity), its lower κ limits any energy waste by dissipation. Accordingly, the sudden temperature increase observed with **1** (Figure 3B) can be explained as a more rapid and effective heating of DU once methanation starts (heat harvesting). On the contrary, the higher C_p value of γ-Al$_2$O$_3$ and its higher κ-value (Table 1) largely mitigate any energy/heat

ChemSusChem

Research Article
doi.org/10.1002/cssc.202201859

Chemistry Europe
European Chemical
Societies Publishing

harvesting phenomena so that only a more gradual T_C increase is observed (Figure 3C).

The effect of DU on the methanation process is certainly more than that of a "thermal mass" for the "heat harvesting" as described above. Indeed, the performance of **1** is superior to that of **3** whatever the operative temperature at the catalyst bed (T_C). As Figure 3B shows, when T_F was set to 250 °C, T_C on **1** grows up to 305 °C and CO_2 conversion (X_{CO_2}) approaches 95 %. With **3**, a T_C value of 305 °C is registered for a T_F setting of 280 °C (Figure 3C). At this T_F value, X_{CO_2} on **3** decreases over 35 % with respect to **1** and lays close to 60 % (Figure 3A). This important activity gap becomes even more relevant when catalysis is operated with the two catalysts (**1** vs. **3**) for a T_F value of 200 °C. Under these conditions, $^{10}Ni/UO_x$ (**1**) reaches X_{CO_2} close to 90 % and an activity gap of 86 % with respect to its γ-Al_2O_3 counterpart (**3**) is measured. To the best of our knowledge, the X_{CO_2} value measured on **1** at T_F setting of 200 °C ($T_C = 260$ °C) is the highest value reported so far in the literature with an unpromoted nickel catalyst within a formally low-temperature methanation run (Table S1).

Several factors can be claimed to explain the superior performance of **1** vs. **3**, such as (1) the increase of the carrier surface alkalinity; (2) a hetero-element doping of the nickel active phase; (3) the generation of more active Ni-UO_x interphases, or a combination thereof. Compared to other ceramics, f-block metal-oxides possess unique electronic structures that can deeply affect the properties of the supported metal active sites. f-Block metal-oxides as supports[53] or dopants[32,33] for transition metal-based catalysts have already been recognized as effective promoters in CO_2-to-SNG conversions. Their ability to generate CO_2 concentration gradients at the catalyst surface[54,55] reflects their inherent surface alkalinity and structural defectiveness[56,57] that are distinctive properties for this class of materials. For catalyst **1**, the generation of a highly active phase can be regarded as the result of an extensive migration/segregation of UO_x particles to the outer Ni NPs surface with the formation of Ni/UO_x core–shell-like composites (see below).

The dependence of catalysts performance from the reaction temperature has been finally investigated by analyzing their behavior on a reverse temperature path. This test was basically carried out to assess the catalyst stability under operative conditions where a thermal balance is established between the reaction heat and the gas–solid heat exchange. Therefore, after reaching the highest λ values, T_F was reduced stepwise to room temperature and X_{CO_2} and T_C were measured after stabilization. Forth and back reaction profiles were almost superimposable with both catalysts (Figure 3A) except for a minor (and negative) hysteresis loop measured on **3**, showing a slight reduction of the process rate (λ) during the cooling phase (Figure 3A, light orange area). Such an effect was attributed to the lower stability of Ni NPs on γ-Al_2O_3 under continuous flow and higher-temperature conditions where metal sintering or leaching phenomena are more likely to occur. Noteworthy, such a negative trend has never been observed on UO_x-based catalyst **1**. Indeed, if generation of Ni/UO_x core–shell-like particles (see below) is thought to prevent undesired Ni-

sintering phenomena, Ni doping by actinide oxides is supposed to stabilize the catalyst under high-temperature gas-phase conditions.[33]

As an additional experiment, **1** and **3** have been studied again as a function of the reactor temperature setting (T_F) but under a doubled GHSV of reagents stream (20000 mL g^{-1} h^{-1}). Figure 4 illustrates the distinctive behavior of **1** from its γ-Al_2O_3-counterpart (**3**) in a complete forth and back temperature cycle. The trends of T_C vs. T_F measured on **1** and **3** within the respective methanation trials are illustrated in Figure 4B,C.

Remarkably, the process ignition on **1** appears even more sharp compared to that observed when the catalyst was operated at 10000 mL g^{-1} h^{-1} as GHSV, and it occurs by increasing the furnace temperature setting (T_F) by very few degrees Celsius. The reaction starts suddenly, and the temperature gap measured between the reactor (T_F) and the catalyst (T_C) increases of about 125 °C within few seconds. At the same time, X_{CO_2} increases from 14 to 93 % while maintaining the process selectivity constant to 100 %. S_{CH_4} plots are shown in the Supporting Information (Figure S6) for the sake of completeness. It should be noticed that with a formal temperature setting of 195 °C (T_F) λ increases on **1** over 1.65 whereas **3** is almost inactive under the same reactor temperature. With **3**,
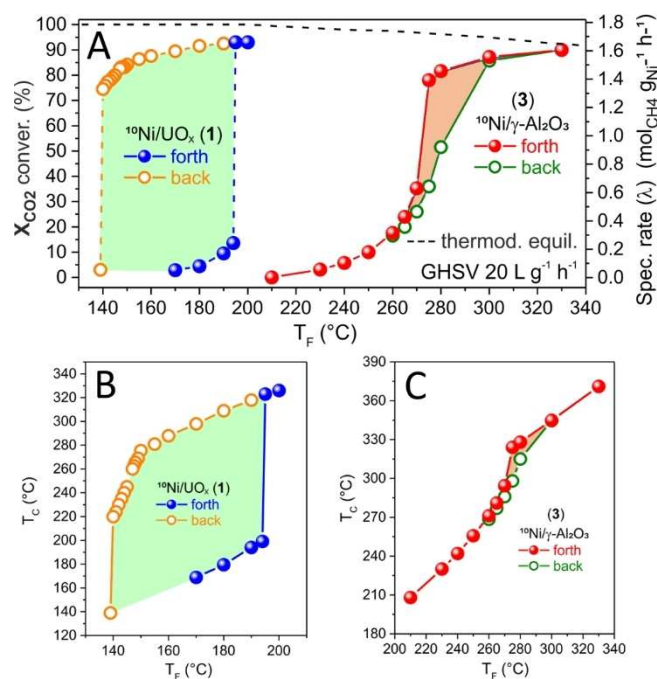
Figure 4. (A) CO_2 methanation with $^{10}Ni/R$ [R = UO_x (**1**) or γ-Al_2O_3 (**3**)] as a function of the reaction temperature (T_F). All catalysts were tested without any thermic diluent using the following reaction conditions: catalyst weight = 500 mg, GHSV (STP) = 20000 mL g^{-1} h^{-1}, [CO_2] = 20 vol%, [H_2] = 80 vol%, H_2/CO_2 = 4, total flow rate = 166.7 mL min^{-1}, atmospheric pressure. Full and empty spheres refer to the forth and back temperature scan, respectively. CH_4 selectivity (S_{CH_4}, not shown in figures) was constantly 100 % in the whole temperature range. The dashed black line refers to the conversion at the thermodynamic equilibrium. Forth and back methanation profiles of **1** and **3** were recorded within 10–12 h and each temperature value was left to stabilize not less than 30 min before recording the data. (B,C) Variation of the temperature values experimentally recorded at the catalyst bed (T_C) vs. those measured at the furnace walls (T_F).

ChemSusChem

Research Article
doi.org/10.1002/cssc.202201859

Chemistry
Europe
European Chemical
Societies Publishing

CH_4 detection started only when the reactor temperature (T_F) reaches 220°C.

This reactivity gap between **1** and **3** better illustrates the net-superior performance of Ni/UO$_x$ catalysts for CO_2 methanation under mild operative temperature conditions. Similarly, the process ignition on **1** suddenly increases the average catalyst temperature (T_C) to values much higher than those settled at the reactor walls (T_F) (Figure 4B). Expectedly, this phenomenon is clearer when the process is operated at higher GHSV. The higher the latter the higher the evolution of extra heat at the catalyst bed per unit of time. Interestingly, higher GHSV ensures a heat harvesting/evolution at the catalyst bed that is superior to the heat removal operated by the classical gas–solid exchange phenomenon. Again, a more gradual increase of the temperature gap between T_F and T_C was measured on **3** under the same experimental conditions (Figure 4C).

When the reaction is operated with **1** at 20000 mL g^{-1} h^{-1} as GHSV, the complete forth and back temperature cycle has unveiled an unexpected phenomenon, not observed with **3** under identical operational conditions. Indeed, once both catalytic systems reach their highest λ value and the reactor temperature is reduced step-wise, DU-based system **1** follows a distinctive behavior that we have arbitrarily named as "quasi autothermal methanation". During the cooling phase, both catalytic systems are allowed to stabilize to constant X_{CO_2} and temperature (T_C and T_F) values (Figure 4). Worthy to note, **1** retains markedly higher performance (X_{CO_2} and λ) compared to that measured with the same catalyst during the heating path at the same reactor temperature settings (T_F). As Figure 4B shows, when T_F decreases down to 190°C, T_C is maintained at 318°C and remains constant for hours. Accordingly, the back-forth temperature swing generates an important X_{CO_2} gap on **1**. For the same reactor temperature setting (T_F), X_{CO_2} on **1** varies from 9.5% ($T_F = 190$°C; $T_C = 194$°C; heating path) to 92.5% ($T_F = 190$°C; $T_C = 318$°C; cooling path) (Figure 4A). Accordingly, the heat required for the process during the cooling path is only partially supplied by the external heater. The extra heat generated on **1** by the reaction exothermicity is unambiguously the main and almost prevalent energy source at the catalyst bed for sustaining the CO_2-to-CH_4 conversion.

To the best of our knowledge, this is the first example of an autothermal methanation process operated on a H$_2$/CO$_2$ fed catalyst in a fixed-bed reactor. Fukuhara et al. have recently referred to autothermal methanation conditions but co-feeding their Ni-based catalysts on different metal oxides with a H$_2$/CO$_2$ mixture containing variable vol% of oxygen (1–10 vol%).[58,59] In this case, the authors claimed the use of hydrogen combustion heat originated at the catalyst surface as the primary heating source to auto-thermally sustain the methanation process.

By reducing the reactor temperature (T_F) on **1** down to 180 or 170°C, T_C passes from 309 to 298°C and a remarkable X_{CO_2} gap (>85%) between the forth and back reaction profiles is maintained. A further decrease of the reactor temperature (T_F down to 140°C) causes the progressive reduction of the catalyst performance with a sudden process switch-off when the external heater setting passes from 141 to 139°C. Accordingly, the back temperature path realizes a large and positive

hysteresis loop (green portion in Figure 4A,B) that reflects the ability of DU-based catalyst **1** to control and usefully reuse the waste heat coming from the process exothermicity.

It should be mentioned that temperature hysteresis in fixed bed catalytic reactors is a well-known phenomenon. It is associated to ineffective heat removal paths for a given catalytic system (active phase + support)[60] and is generally regarded as a detrimental if not highly risky phenomenon, responsible for the premature catalysts deactivation or even reactor thermal explosion.[61]

On the other hand, a recent in silico study by Bremer and Sundmacher has predicted possible stabilization concepts for unstable operational regimes in fixed-bed reactor models engaged for CO_2 methanation at the industrial scale.[62] Their reactor concept based on thermal feedback generated from "controlled hot-spots" highlights the importance of heat diffusion control and material heat capacity as key features to be optimized for the stabilization of hysteresis loops. This reactor model that turns waste energy back into useful energy for catalysis fits well with the experimental outcomes of our Ni/UO$_x$ catalysts.

An additional proof of the improved catalyst performance at higher GHSVs is offered by comparing **1** at the limit T_F setting of 141°C and 20000 mL g^{-1} h^{-1} as GHSV. When T_F is reduced to this limit value, T_C remains at 220°C (Figure 4B) and X_{CO_2} lays closely to 75%. At GHSV of 10000 mL g^{-1} h^{-1}, $T_C = 220$°C is reached for a reactor temperature setting (T_F) of around 197°C (Figure 3B) and X_{CO_2} is nearly reduced by a half (≈ 38%; Figure 3A).
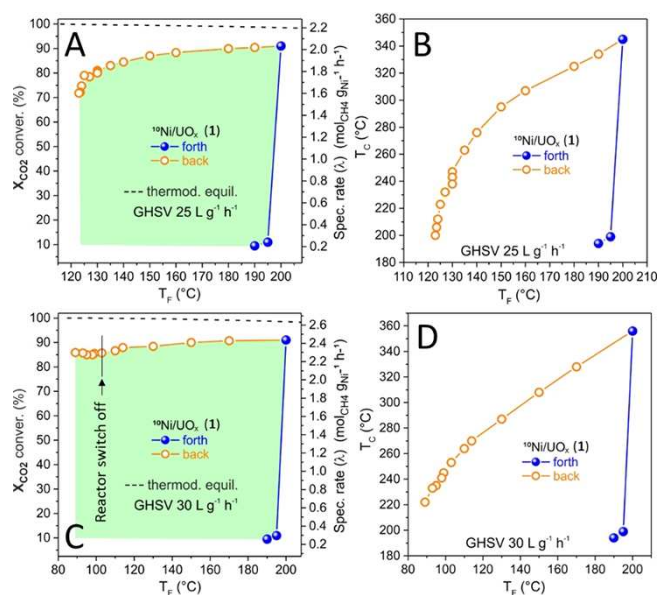
Overall, this catalytic behavior significantly improves the efficiency of the methanation process and reduces the amount of external energy/heat employed for the process to occur. It is also important to note that **1** entirely recovers its reactivity profiles (Figure 4A) once operated in successive methanation runs within similar forth and back temperature cycles. This highlights the excellent stability of the catalytic system under operative conditions and proves that the generation of hysteresis loops is not ascribed to any irreversible modification of the catalytic active phase.

In addition, it is important to note that the appearance of a positive hysteresis loop on **1** cannot be simply attributed to an effect of the adiabatic nature of the reactor setup. Indeed, the same forth and back reactivity trend measured on the benchmark ^{10}Ni/γ-Al$_2$O$_3$ (**3**) (Figure 4A, right side hand, and Figure 4C) does not show any positive hysteresis during the cooling path. Once again, **3** operating at 20000 mL g^{-1} h^{-1} as GHSV shows a negative loop, whose appearance is attributed to a partial catalyst deactivation during the back-temperature path.

Doubling the reagents rate from 10000 to 20000 mL g^{-1} h^{-1} appears crucial to feed the hysteresis loop and to unveil the unique and distinctive properties of DU-based catalysts. When catalysis with **1** is operated at GHSV = 25000 and 30000 mL g^{-1} h^{-1}, even more pronounced stable and durable hysteresis loops are formed during the reactor cooling phase (Figure 5A,C).

Whatever the reagents' flow rate, S_{CH_4} remains constantly to 100% (Figure S7). As Figure 5A,C shows, the process ignites

ChemSusChem

Research Article
doi.org/10.1002/cssc.202201859

Chemistry Europe
European Chemical
Societies Publishing

Figure 5. CO_2 methanation with catalyst **1** as a function of the reaction temperature (T_F), at (A) 25000 and (C) 30000 $mL\,g^{-1}\,h^{-1}$ as GHSV, respectively. All other reactional details are the same reported in the caption of Figure 4A. Light-green areas refer to the observed positive hysteresis loops. The dashed black line refers to the conversion at the thermodynamic equilibrium and has been included in (A) and (C) for the sake of completeness. Full and empty spheres refer to the forth and back temperature scan, respectively. CH_4 selectivity (S_{CH_4}, not shown in figures) was constantly equal to 100% in the whole temperature range. Forth and back methanation profiles were recorded within 10–12 h and each temperature value was left to stabilize not less than 30 min before recording the data. (B,D) Variation of the temperature experimentally recorded at the catalyst bed (T_C) vs. that measured at the furnace walls (T_F).

very quickly and approaches λ values as high as 2.05 and 2.46 $mol_{CH_4}\,g^{-1}\,h^{-1}$ for 25000 and 30000 $mL\,g^{-1}\,h^{-1}$ as GHSV respectively, already at a reactor temperature (T_F) of 200°C. The reduction of the reactor temperature (T_F) is accompanied by λ values that remain constantly high within a relatively large range of low T_F values.

It should be noticed that the higher the GHSV, the lower the dependence of λ from the decrease of the reactor temperature (T_F). This is clearly outlined in the more linear and constant trend observed for λ values recorded during the back-temperature path on **1** at 30000 $mL\,g^{-1}\,h^{-1}$ as GHSV (Figure 5C vs. A). Noteworthy, after reducing T_F setting down to 103°C, the external heating was definitively switched off (Figure 5C) while constantly feeding the catalyst bed with the reagents stream. Under these conditions, T_C stabilizes gradually to 220°C and λ lays constantly (for hours) close to 2.32 $mol_{CH_4}\,g^{-1}\,h^{-1}$. It should be noticed that during this phase, T_F remains close to around 80 ± 5°C due to a heat radiation effect from the hot quartz tube reactor. This finding represents a unique but concrete example of CO_2-to-CH_4 catalytic conversion operated under a true autothermal methanation regime.
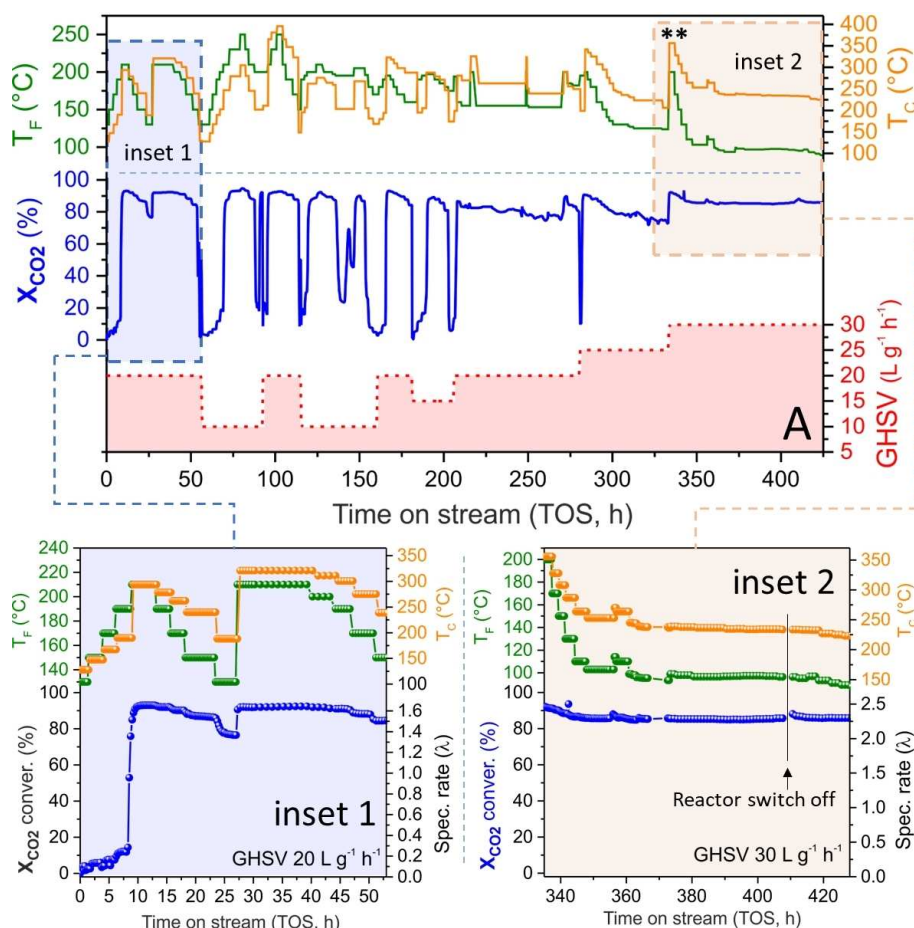
1 has finally been employed in an exceptionally long-term methanation test (> 400 h, > 16 days) in order to evaluate its stability upon discontinuous operational conditions. A freshly prepared sample of **1** was then operated under a constant H_2/

CO_2 gas stream (4 v/v) at ambient pressure while GHSV was randomly varied between 10000 and 30000 $mL\,g_{cat}^{-1}\,h^{-1}$. At the same time, the reactor temperature (T_F) was varied, up and down, within the 80–250°C temperature range and the corresponding T_C values were recorded upon stabilization. Figure 6 illustrates the different stages of the long-term test, and its analysis offers several hints to the discussion on the catalyst performance beyond its inherent stability on long-term runs.

Top side of Figure 6A illustrates the gap between the reactor temperature setting (T_F) and that recorded at the catalytic bed (T_C) as a function of the reagents' flow rate (GHSV, red curve on the bottom side of Figure 6A). After around 25 h on stream, T_C vs. T_F excursions appear fully consistent with the trends discussed above on Figures 3B, 4B, and 5B,D. On the other hand, inset 1 of Figure 6A exhibits a dynamic evolution of the catalytic phase during the first hours on run. Indeed, after 10 h, T_F is set at 210°C and T_C stabilized around 293°C. Afterwards, T_F was reduced stepwise to 130°C before being increased again to 210°C ($\approx$30 h). At this stage, T_C increased up to its regime temperature value ($\approx$320°C), perfectly in accord with the T_F vs. T_C trend measured for **1** under identical operative conditions (see Figure 4B). However, such a stabilization to regime conditions (not appreciable in terms of X_{CO_2}), suggests that a sort of rearrangement of the catalyst active phase takes place during the first hours on run. Such a rearrangement is attributed to the above-mentioned segregation of uranium-oxide particles to the outer Ni NPs surface with the subsequent generation of Ni/UO_x core–shell-like composites (see below).

From 50 to 330 h on stream, the catalyst undergoes variable experimental conditions in terms of reactor temperature setting (T_F) and reagents' flow rate (GHSV). All over the methanation test, **1** exhibits outstanding stability without any apparent deactivation or alteration of its pristine performance. During the last 100 h on run (inset 2), the reactor temperature (T_F) is set at 200°C (** in Figure 6A) and **1** is allowed to stabilize under 30000 $mL\,g^{-1}\,h^{-1}$ as GHSV. Under these conditions, the catalyst temperature (T_C) increases rapidly to around 355°C (see also Figure 5D) and X_{CO_2} stabilizes to 92%. Afterwards, T_F was decreased down to 100°C and T_C stabilizes to 230–240°C.

Under these conditions, **1** ensures a X_{CO_2} close to 85% that remains constant for more than 80 h. After 410 h, the reactor heating is deliberately switched off and the process monitored again for further 20 h. Remarkably, these last operational conditions perform CO_2 methanation efficiently without the contribution of any external heating supply. The extra heat developed by the process exothermicity at a constantly fed catalytic bed (reagents flow rate 30000 $mL\,g^{-1}\,h^{-1}$), is harvested and efficiently reused back to run the reaction under an autothermal regime. It should be noticed that during autothermal conditions (external heating source switched off), T_F maintains around 80 ± 10°C as the result of the radiation heat from the quartz tube reactor whose core temperature (T_C) constantly lays on around 220°C (inset 2). S_{CH_4} is regularly measured during the process but for the sake of shortness Figure S7 (Supporting Information) lists the selectivity values for the first two and the last five days only. As it can be seen from

ChemSusChem

Research Article
doi.org/10.1002/cssc.202201859

Chemistry
Europe
European Chemical
Societies Publishing

Figure 6. Long-term methanation test with **1** under variable GHSVs (from 10000 to 30000 mL g^{-1} h^{-1}) and reactor temperature (T_F) settings. (A) Catalyst performance (X_{CO_2}) recorded under variable experimental conditions using a constant H_2/CO_2 gas stream (4 *v/v*) at ambient pressure. CH_4 selectivity (S_{CH_4}, not shown in figures) was constantly equal to 100% throughout the whole long-term test (>440 h; >16 days). Insets 1 and 2 highlight two distinctive features of **1** throughout the whole stress-test.
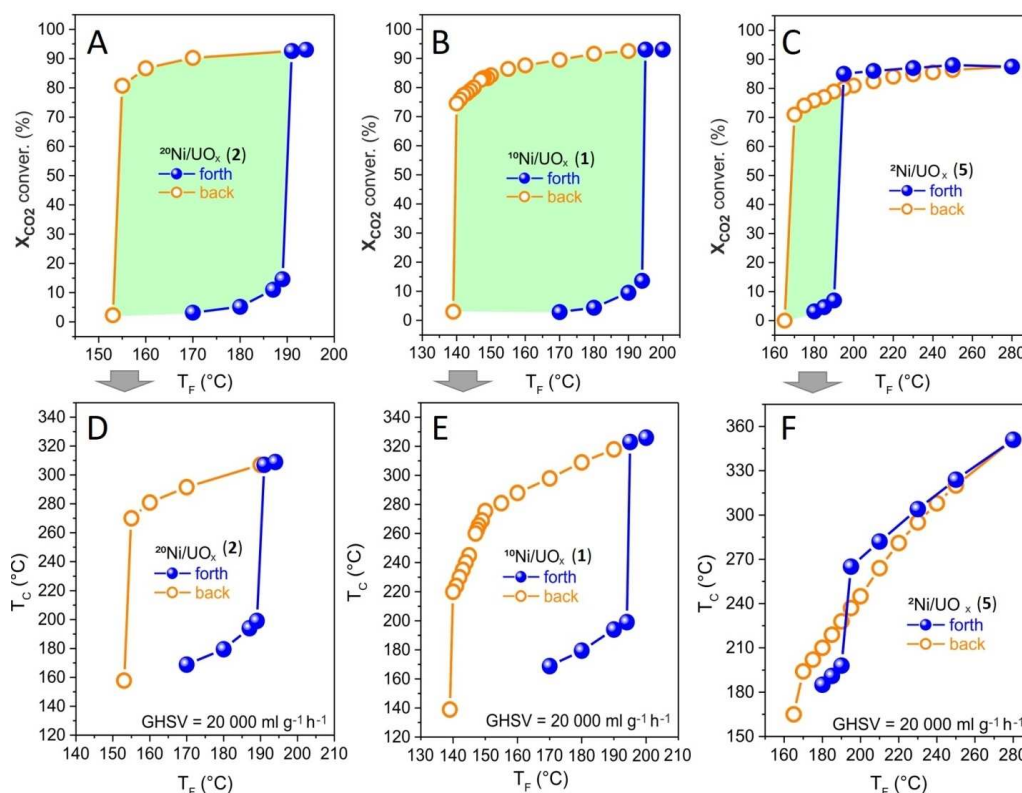
this Figure, selectivity is maintained to 100% all over the long-term test.

Influence of nickel loading on the performance of Ni/UO$_x$ catalysts

The influence of the nickel loading on CO_2 methanation with ^{k}Ni/UO$_x$ composites has been accomplished by comparing the performance of **1** with those of catalysts **3** and **5** containing two-fold (20 wt%) and one-fifth (2 wt%) loading of the nickel phase, respectively. For all these systems, methanation is operated under the experimental conditions that better illustrate the quasi-autothermal regime recorded with **1**. Accordingly, experiments have been carried out using a H_2/CO_2 ratio of 4 (*v/v*), at ambient pressure and 20000 mL g^{-1} h^{-1} as GHSV. Figure 7A–C illustrates the performance of the three catalysts at comparison as a function of the reaction temperature in the whole forth and back scan of temperatures range. Figure 7D–F finally reports the variation of T_C vs. T_F for the complete thermal cycles.

All catalytic runs start within almost the same narrow T_F range comprised between 190 and 195 °C (Figure 7A–C). While T_C values measured on **1** and **2** raise suddenly over 300 °C and X_{CO_2} on both catalysts ranks close to 93% (Figure 7D,E, close to the thermodynamic equilibrium), T_C on the low-charged catalyst **5** increases up to 265 °C and X_{CO_2} stabilizes on slightly lower conversion values ($\approx 85\%$, Figure 7C,F). Doubling the nickel content (**2** vs. **1**) does not change appreciably the catalyst performance in terms of temperature setting (T_F) vs. X_{CO_2} and T_C values measured at the catalytic bed. On the other hand, the relatively high performance of **5** (Ni = 2 wt%) with a X_{CO_2} of 85% and $S_{CH_4} = 100\%$ (Figure S8) already for temperature values (T_F) as low as 195 °C deserves to be pointed out. This performance corresponds to a process rate (λ) of 6.77 mol$_{CH_4}$ g$_{Ni}^{-1}$ h^{-1} that to the best of our knowledge ranks among the highest methanation performance reported so far for nickel catalysts containing such a low metal loading and operated under low-temperature conditions (see also Table S1).

As far as catalysts behavior during the reactor cooling path is concerned, all of them exhibited a clear hysteresis trend with distinctive features (Figure 7A–C). Doubling the nickel loading

ChemSusChem

Research Article
doi.org/10.1002/cssc.202201859

**Chemistry
Europe**
European Chemical
Societies Publishing

Figure 7. (A–C) CO_2 methanation under variable reaction temperatures with catalysts **2** (20 wt% of Ni), **1** (10 wt% of Ni), and **5** (2 wt% of Ni). Exact nickel charge is reported in Table 2. (D–F) Temperature variation at the catalyst bed (T_C) vs. the furnace walls temperature setting (T_F). Other reaction conditions: 500 mg of each catalyst, $H_2/CO_2 = 4$ (v/v), ambient pressure, and GHSV = 20000 mL g^{-1} h^{-1}.

(**2**) did not translate into superior catalyst performance respect to **1**, neither during the heating path nor when the catalyst is operated under quasi-autothermal conditions (cooling reactor phase).

2 formally switches off ($X_{CO_2} < 3\%$) when the reactor temperature (T_F) drops below 155 °C ($T_C = 270$ °C) (Figure 7A,D) whereas **1** still retains a relatively high X_{CO_2} ($\approx 75\%$) at a reactor temperature (T_F) of 140 °C ($T_C = 220$ °C) (Figure 7B,E). The reduced performance of **2** is attributed to nickel particles overcrowding on the macroporous and low surface area ceramic that limits the synergistic Ni/UO$_x$ interactions. In addition, a too high-nickel loading can affect the ultimate catalyst density and its associated thermal mass properties, hence modifying its performance (hysteresis loop) during the reactor cooling phase.
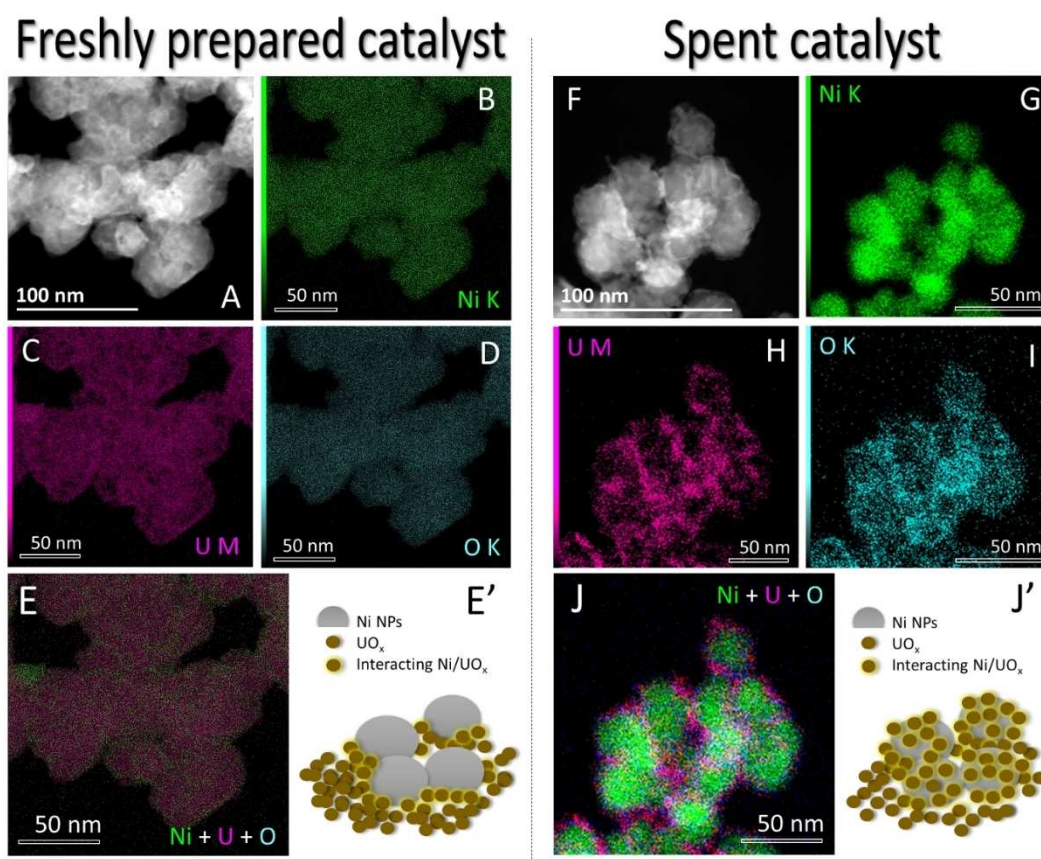
A reduced nickel loading (**5**, Ni = 2 wt%) results into a less marked hysteresis loop too (Figure 7C). The lower "extra heat" generated at the catalytic bed by the reduced charge of active sites smooths the temperature gap (T_F vs. T_C) during the reactor cooling phase (Figure 7F). As a result, X_{CO_2} drops down suddenly for methanation operated under quasi-autothermal regime once the furnace temperature (T_F) is reduced below 170 °C. On the other hand, it should be noticed that when **5** stabilizes at $T_F = 175$ °C (under the quasi-autothermal regime), T_C lays around 202 °C and X_{CO_2} approaches around 75% (Figure 7C,F). With 10 wt% of Ni NPs in **1**, a X_{CO_2} conversion of around 75% is

obtained under quasi-autothermal conditions (reactor cooling phase) for a catalyst temperature (T_C) about 20 °C higher (Figure 7B,E). The formal reduction of T_C in **5** is certainly ascribable to a superior nickel active phase dispersion on the oxide matrix that facilitates in turn more extensive Ni/U interactions (see below).

Generation of Ni/UO$_x$ core–shell-like methanation catalysts

The generation of a highly active and durable catalytic phase in DU-based Ni-catalysts was associated to the migration/segregation of UO$_x$-particles to the outer Ni NPs surface. Such a phenomenon generates Ni/UO$_x$ core–shell-like composites where distinctive features of f-block oxides and Ni active particles are emphasized. Although this physical rearrangement is likely to start already during the catalyst synthesis, the comparative analysis of heavy elements distribution in the freshly prepared catalyst and its used counterpart (after a long-term methanation cycle), better illustrates the occurrence of this phenomenon. To this end, a comparative high-angle annular dark-field (HAADF)-STEM analysis combined with EDS has been carried out on DU-based system **1** before and after the long term (> 400 h) methanation test.

At odds with the freshly prepared catalyst (Figure 8A–D), its recovered counterpart (Figure 8F–I) shows the formation of Ni/

ChemSusChem

Research Article
doi.org/10.1002/cssc.202201859

Chemistry Europe
European Chemical
Societies Publishing

Figure 8. (A,F) HAADF-STEM images and their EDS analyses of **1** (A–E) before and (F–J) after a long-term (400 h) methanation run. Ni and U species (B,C and G,H) were detected from the X-ray signals at the Ni–K and U–M edge on the fresh (left-hand side) and exhaust (right-hand side) catalyst, respectively. (E) and (J) refer to the overlay of Ni K edge, U M edge, and O K edge, and illustrate the core–shell-like structure in the used catalyst **1**. (E′) and (J′) refer to the schematic representation of U and Ni on fresh and spent catalysts.

UO_x core–shell-like networks as the result of the aforementioned segregation of UO_x particles around larger Ni NPs aggregates (Figure 8E,E′ vs. J,J′).

As Figure 8E shows, Ni and U particles are homogeneously distributed on the freshly prepared system whereas UO_x creates like an outer shell for the nickel phase after catalysis (Figure 8J). Low-nickel-loaded samples (e.g., **5**) show even better the occurrence of this UO_x particles segregation process. As Figure S9 (Supporting Information) shows, nickel phase appears homogeneously distributed at the surface of larger UO_x portions whereas smaller particles of uranium oxide segregate all around the edges of larger nickel aggregates.

Such a phenomenon has related precedents from the literature,[63] and it can be conveniently explained on the basis of a very recent study on the metal–support interplay in classical noble-metal-based heterogeneous catalysts of the state-of-the-art. Willinger and co-workers have reported an elegant in-situ HRTEM study describing a dynamic structural transformation of a Pt/TiO_2 catalyst under redox conditions.[64] They observed the encapsulation of their noble-metal particles by TiO_2 when the catalyst was employed under a reducing environment. Accordingly, our reducing environment replicates

a similar migration/segregation phenomenon to that observed with Pt/TiO_2.

It should also be mentioned that UO_x migration favors a more extensive Ni/U interaction (Figure 8E′,J′) hence emphasizing the non-innocent role of electron-rich f-block metal-oxides as either supports[53] or dopants[32,33] for Ni NPs. Finally, UO_x migration is thought to create a physical barrier that serves to mitigate or even prevent undesired sintering and leaching phenomena of Ni NPs. This evidence explains the remarkable stability and durability of Ni/UO_x in long-term methanation trials.

For the sake of completeness, metals oxidation state and composition of the fresh (**1**) and used catalyst (**1′**) were analyzed by XPS and ICP-AES, respectively. XPS survey spectra (Figure S10) highlight that samples namely contain nickel,[65] uranium,[66] and oxygen. A comparative analysis of high-resolution U 4f and Ni 2p core regions recorded on the freshly prepared and on the recovered catalyst has shown almost superimposable profiles, hence ruling out any significant alteration in the oxidation state of heavy elements. Finally, ICP-AES analysis of **1** and **1′** highlighted the outstanding stability/durability of the former throughout the methanation process. As Table 2 shows (entry 2 vs. 1), a negligible 3.3 % of nickel was

ChemSusChem

Research Article
doi.org/10.1002/cssc.202201859

Chemistry Europe
European Chemical
Societies Publishing

formally leached in **1'** after more than 400 h on run. This evidence is in line with the high performance of **1** throughout the whole methanation test, and its highly responsive behavior to all variable operational conditions adopted during such an exceptionally long methanation trial.

Conclusions

To summarize, we reported on the straightforward synthesis of Ni-catalysts using the less conventional depleted uranium (DU) oxides (UO_x) as a support to give a unique class of highly efficient, selective and durable systems for the low-temperature CO_2-to-CH_4 conversion. These findings outline a breakthrough in a challenging research field at the heart of power-to-gas technology while providing at the same time useful hints to address severe environmental concerns.

Besides the superior performance of Ni/UO_x catalysts with respect to their benchmark Ni/γ-Al_2O_3 counterparts, the high density of UO_x along with its low specific heat capacity (C_p) and thermal conductivity (κ) make it a unique vector for running exothermic transformations. Indeed, Ni/UO_x composites join together the properties of an outstanding methanation catalyst with those of an ideal adiabatic setup. As for the latter feature, they allow an effective harvesting of the extra-heat originated by the methanation exothermicity turning it back into useful energy for the process itself. The appearance of net and positive hysteresis loops in the catalyst specific rate (λ) upon decreasing the reactor temperature setting (T_F) implies that the reaction exothermicity (constantly fed by reagents flow) is the main and almost self-sustaining heating source engaged for the CO_2-to-CH_4 conversion. Accordingly, DU deeply impacts on the ultimate catalyst performance and the process sustainability, acting as a f-block dopant for the nickel phase and thermal mass for the mitigation of energy wastes at the same time. While f-block doping translates into a significant intensification of the low-temperature methanation, thermal mass strongly and positively affects the overall energy balance of the process.

A comparison of Ni/UO_x catalysts with their benchmark Ni/γ-Al_2O_3 counterparts, operated under identical conditions, has systematically been employed as a proof of evidence for the much higher performance of the former. In addition, it has also been used to confirm that positive hysteresis loops on Ni/UO_x catalysts are not accidentally ascribed to the adiabatic nature of the reactor setup.

The unique properties of Ni/UO_x catalysts have finally been demonstrated in a series of seminal catalytic runs operated under exceptionally low reactor temperature settings (T_F) and under a quasi-autothermal methanation regime. Finally, an exceptionally long-term methanation run (>400 h, >16 days) has been carried out to demonstrate the stability and durability of Ni/UO_x catalyst **1** and to make it operating under truly autothermal conditions [i.e. when the external heating source (T_F) was definitively switched off].

Besides the merits of the proposed catalytic technology applied to a challenging and environmentally "net zero-impact" process, it also proposes an original approach to recycle and bring to a second life a nuclear by-product, providing a valuable alternative to its more costly long-term storage or controlled disposal.

Experimental Section

Synthesis of ^{k}Ni/R composites

In a typical procedure, γ-Al_2O_3 (Ketjen CK-300B, Akzo Nobel, $S_{BET}=279\pm10$ $m^2 g^{-1}$) in the form of extruded trilobes (≈1 mm$\times1$ mm) or U_3O_8 powder (Prolabo, France; $S_{BET}\approx1$ $m^2 g^{-1}$) were impregnated with $Ni(NO_3)_2\cdot6H_2O$ (Fluka) aqueous solutions at variable salt concentrations. In the case of U_3O_8 powder it was previously shaped in the form of grains (≈0.8 mm) using water spheronisation technique. Samples were calcined afterwards in air at 350 °C before being used for the subsequent impregnation step. For each sample, the volume of aqueous Ni salt solution was significantly higher than the total pore volume of the selected support and the Ni content was initially established on the basis of the expected final metal loading. Suspensions were evaporated and samples oven-dried at 120 °C for 2 h before being calcined in air at 350 °C for 2 h (heating rate for drying and calcination: 3 °C min^{-1}) as to convert the nickel salt into the corresponding nickel oxide. The as-obtained ^{k}NiO/R pre-catalysts ($k=2$, 10, or 20 wt%) were converted into their ^{k}Ni/R [R=UO_x (**1**, **2**, **5**), γ-Al_2O_3 (**3**, **4**)] counterparts under a pure H_2 flow (100 mL min^{-1}) at 350 °C for 2 h just before undergoing CO_2 methanation tests.[36] ***CAUTION!!!*** *All thermal treatments and samples manipulation were carried out in a dedicated setup as to avoid any external contamination by UO_x even in traces. Personal protective equipment, such as FFP3 protection masks and double gloves were also worn by the manipulator. All technical stuffs and disposable materials were stored in a sealed container that was shipped back to a dedicated waste treatment centre of ORANO.*

The nickel loading was determined on each sample by ICP-AES analysis, and it was fixed as follows: **1**: ^{10}Ni/UO_x (ICP: 9.91 wt%); **2**: ^{20}Ni/UO_x (ICP: 17.52 wt%); **3**: ^{10}Ni/γ-Al_2O_3 (ICP: 8.60 wt%); **4**: ^{20}Ni/γ-Al_2O_3 (ICP: 18.77 wt%), and **5**: ^{2}Ni/UO_x (ICP: 2.24 wt%). Catalyst productivity (see below) expressed as mol_{CH_4} g_{Ni}^{-1} h^{-1} (λ) has been calculated assuming the exact nickel loading (ICP-determined) while the theoretical Ni-content was arbitrarily maintained in the catalyst name. A summary of the nickel content in the five newly prepared catalysts (**1**–**5**) is outlined afterwards in Table 2.

### Characterization methods

PXRD measurements were carried out on a Bruker D-8 Advance diffractometer equipped with a Vantec detector (Cu K$_\alpha$ radiation) working at 40 kV and 40 mA. X-ray diffractograms were recorded in the 20–90° 2θ region at room temperature in air. TEM was carried out on a JEOL ARM-200F working at 200 kV accelerated voltage, equipped with a probe corrector for spherical aberrations and a point-to-point resolution of 80 pm. Elemental mapping was accomplished by STEM on a JEOL ARM-200F electron microscope equipped with a Gatan Energy Filter and a cold field-emission gun (FEG) operated at 200 kV with 1.5 Å lattice resolution. For these measurements, samples were dispersed by ultrasounds treatment (5 min) in chloroform or ethanol and drop casted on a copper grid covered with a holey carbon membrane for observation. Elemental signals were extracted from the Al–K, Ni–K, U–M, O–K, and Ni/O/Al–K, U–M ionization edges. The BET SSAs were calculated from N_2 (**3**, **4**) or Kr (UO_x, **1**, **2**, and **5**) physisorption isotherms recorded at the temperature of liquid N_2 (77 K) on an ASAP 2020 Micromeritics instrument. Pore size distribution was determined by Barrett–

ChemSusChem

Research Article
doi.org/10.1002/cssc.202201859

Chemistry Europe
European Chemical
Societies Publishing

Joyner–Halenda (BJH) method for samples **3** and **4**. Whatever the physisorption analysis (N_2 or Kr), all samples were degassed/activated at 250 °C for 6 h before measurement. Nickel surface areas (S_{Ni}, $m^2 g_{Ni}^{-1}$) and metal dispersions (*D*, %) were determined by H_2 chemisorption conducted on an ASAP 2020 Micromeritics instrument. Samples were pre-treated in a H_2 flow for 2 h at 350 °C and adsorption isotherms were recorded at 35 °C. The Ni surface area was determined from the total amount of adsorbed H_2 extrapolated to zero pressure after subtracting the contribution of physisorbed H_2, assuming a Ni/H = 1 stoichiometry and a 6.49 Å^2 nickel cross-sectional area. ICP-AES measurements on the mineralized pre-catalysts ^{k}NiO/γ-Al_2O_3, ^{k}NiO/UO_x, and on the used catalyst **1'** were accomplished on a Varian 720 ES ICP-AES instrument.

Catalytic tests

CO_2 methanation reaction [Eq. (1)] was carried out at atmospheric pressure in a MCB system (The Micro Catalyst Bed unit, VINCI Technologies, France) using a fixed-bed quartz tubular reactor [$Ø_{ED}$ = 10 mm, $Ø_{ID}$ = 6 mm, length = 400 mm] charged with 0.5 g of catalysts **1–5** ($V_1 = V_2 = V_5 \approx 0.155$ cm^3; $V_3 = V_4 \approx 0.34$ cm^3) and housed in an adiabatic electrical furnace. ***Notation!!!*** *The catalytic setup was placed in a home-made plexiglas-sealed box whose gas outlet was passed through a two-stage filter (quartz wool and activated charcoal) for trapping any trace of solid products before releasing reaction effluents to the central filtration/evacuation system.*

$$CO_2 + 4H_2 \rightarrow CH_4 + 2H_2O; \ \Delta H = -165 \ kJ\,mol^{-1} \quad (1)$$
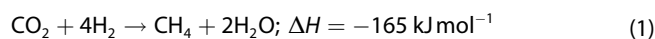
The temperature of the system was monitored by three type-K thermocouples ($Ø_{ED}$ = 0.5 mm). Two of them were located in close proximity to the quartz tube borders and used for regulating the oven temperature (T_F). The third one was placed in the middle of the catalytic bed (T_C) for measuring the temperature swings (T_C vs. T_F) throughout the process (see Figure S1). Just prior of each methanation run, pre-catalysts were reduced under a stream of pure hydrogen (100 mL min^{-1}) for 2 h at 350 °C. Afterwards, each catalyst was allowed to reach and stabilize (30–45 min) at the target temperature under a pure stream of Ar (max. temperature deviation recorded between T_F and T_C after stabilization ≈ ± 3 °C).

In a typical procedure, a H_2/CO_2 gas mixture (4 *v/v*) regulated at variable GHSVs (from 10000 to 30000 mL $g_{cat}^{-1} h^{-1}$) by a series of calibrated mass flow controllers (Brookhorst) was continuously fed through the catalytic bed maintained at the target temperature. Gases at the reactor outlet were passed through a Peltier cool trap where water was condensed before reaching the gas chromatograph. Reactants and products were analysed on-line by a gas micro-chromatograph (μGC SRA R3000) with two columns for analysis of CO, CH_4, H_2 and CO_2, C_2H_6 respectively, equipped with a thermal conductivity detector (TCD). All reactor exit lines were maintained at 110 °C by external heating tapes in order to avoid condensation of residual water in the feed. CO_2 conversion (X_{CO_2}) and CH_4 selectivity (S_{CH_4}) were calculated according to the following equations [Eqs. (2) and (3)]:

$$X_{CO_2}[\%] = \frac{F_{CO_2(in)} - F_{CO_2(out)}}{F_{CO_2(in)}} \times 100 \quad (2)$$

$$S_{CH_4}[\%] = \frac{F_{CH_4(out)}}{F_{CH_4(out)} + F_{CO(out)}} \times 100 \quad (3)$$

where $F_{x(in/out)}$ [mL min^{-1}] is the flow rate of each component in the gas feed at the reactor inlet or outlet. S_{CH_4} values were constantly 100 % all over the methanation experiments described in the manuscript. Neither CO nor other potential side-products were detected at the reactor outlet all over this experimental work. Accordingly, S_{CH_4} was arbitrarily omitted from Figures in the main document but illustrated in the Supporting Information for the sake of completeness.

Author Contributions

Conceptualization: L. T.-P.; M. A.; G. G. & C. P.-H. Methodology and its development: L.T.-P. J.-M. N.; Validation: Formal analysis: S. S.; G. T.; A. R.; V. P.; C. D.-V.; A. J. & L. V. Investigation: L. T.-P.; M. A.; J.-M. N.; G. G. & C. P.-H. Data Curation: L. T.-P.; M. A.; C. P.; G. G. & C. P.-H. Writing - Original Draft: L. T.-P.; G. G. & C. P.-H. Supervision: Project management/coordination: L. T.-P.; G. G. & C. P.-H. Funding acquisition: G. G. & C. P.-H.

Conflict of Interest

There are no conflicts to declare.

Data Availability Statement

The data that support the findings of this study are available in the supplementary material of this article.

[1] Z. Yan, J. L. Hitt, J. A. Turner, T. E. Mallouk, *Proc. Natl. Acad. Sci. USA* **2020**, *117*, 12558–12563.

[2] J. Artz, T. E. Müller, K. Thenert, J. Kleinekorte, R. Meys, A. Sternberg, A. Bardow, *Chem. Rev.* **2018**, *118*, 434–504.

[3] G. Mantulet, A. Bidaud, S. Mima, *Energy* **2020**, *193*, 116737.

[4] C. Vogt, M. Monai, G. J. Kramer, B. M. Weckhuysen, *Nat. Catal.* **2019**, *2*, 188–197.

[5] A. Kätelhöna, R. Meysa, S. Deutza, S. Suhb, A. Bardow, *Proc. Natl. Acad. Sci. USA* **2019**, *116*, 11187–11194.

[6] C. Hepburn, E. Adlen, J. Beddington, E. A. Carter, S. Fuss, N. Mac Dowell, J. C. Minx, P. Smith, C. K. Williams, *Nature* **2019**, *575*, 87–97.

ChemSusChem

Research Article
doi.org/10.1002/cssc.202201859

Chemistry Europe
European Chemical
Societies Publishing

[7] https://www.eia.gov/uranium/marketing/pdf/2021%20UMAR.pdf (last access June 6th, 2022).

[8] K. Sanyal, A. Khooha, G. Das, M. K. Tiwari, N. L. Misra, *Anal. Chem.* **2017**, *89*, 871–876.

[9] S. A. Katz, *Toxics* **2014**, *2*, 50–78.

[10] Depleted Uranium Inventories: http:// www.wise-uranium.org/eddat. html. Site updated 21 September 2021; Retrieved 01 December 2021.

[11] R. R. Price, M. J. Haire, A. G. Croff, in *Waste Management 2001 Symposium*, Tucson, Arizona, **2001**, p. 8.

[12] G. J. Hutchings, C. S. Heneghan, I. D. Hudsont, S. H. Taylor, *Nature* **1996**, *384*, 341–343.

[13] Z. R. Ismagilov, S. V. Kuntsevich, *Chem. Sustain. Develop.* **2009**, *17*, 439–463.

[14] Z. R. Ismagilov, S. V. Lazarev, *Catal. Rev. Sci. Technol.* **2013**, *55*, 135–109.

[15] D. R. Hartline, K. Meyer, *J. Am. Chem. Soc. Au* **2021**, *1*, 698–709.

[16] E. Lu, S. T. Liddle, *Dalton Trans.* **2015**, *44*, 12924–12941.

[17] S. T. Liddle, *Angew. Chem. Int. Ed.* **2015**, *54*, 8604–8641; *Angew. Chem.* **2015**, *127*, 8726–8764.

[18] M. Falcone, L. Chatelain, R. Scopelliti, I. Živković, M. Mazzanti, *Nature* **2017**, *547*, 332–335.

[19] D. P. Halter, F. W. Heinemann, J. Bachmann, K. Meyer, *Nature* **2016**, *530*, 317–321.

[20] A. R. Fox, S. C. Bart, K. Meyer, C. C. Cummins, *Nature* **2008**, *455*, 341–349.

[21] https://world-nuclear.org/information-library/nuclear-fuel-cycle/ura-nium-resources/uranium-and-depleted-uranium.aspx (last access 18/03/2022).

[22] C. Cantaluppi, S. Degetto, *Annal. Chem.* **2000**, *90*, 665–676.

[23] C. J. Humrickhouse-Helmreich, R. Corbin, S. M. McDeavitt, *J. Nucl. Mater.* **2014**, *446*, 100–105.

[24] I. H. Saleh, *J. Radiat. Res. Appl. Sci.* **2018**, *11*, 182–189.

[25] F. Shaki, E. Zamani, A. Arjmand, J. Pourahmad, *Iran. J. Pharm. Sci.* **2019**, *18*, 90–100.

[26] J. J. Calvin, M. Asplund, Y. Zhang, B. Huang, B. F. Woodfield, *J. Chem. Thermodyn.* **2017**, *112*, 77–85.

[27] J. F. Shackelford, W. Alexander, *CRC Materials Science and Engineering Handbook*, CRC Press, **2001**, pp. 1928.

[28] A. T. Nelson, D. R. Rittman, J. T. White, J. T. Dunwoody, M. Kato, K. J. McClellan, *J. Am. Ceram. Soc.* **2014**, *97*, 3652–3659.

[29] D. de Ligny, P. Richet, E. F. Westrum Jr, J. Roux, *Phys. Chem. Miner.* **2002**, *29*, 267–272.

[30] T. Tojo, T. Atake, T. Mori, H. Yamamura, *J. Chem. Thermodyn.* **1999**, *31*, 831–845.

[31] On a merely physical ground, it can also be stated that the high density of DU-based catalysts allow to operate catalytic processes within more compact reactor setup while ensuring even better performance of those obtained with reactors/catalysts of the state-of-the-art.

[32] J. B. Branco, P. E. Brito, A. C. Ferreira, *Chem. Eng. Sci.* **2020**, *380*, 122465.

[33] J. B. Branco, A. C. Ferreira, *Eur. J. Inorg. Chem.* **2019**, *7*, 1039–1045.

[34] A. C. Ferreira, J. B. Branco, *Int. J. Hydrogen Energy* **2019**, *44*, 6505–6513.

[35] A. C. Ferreira, J. B. Branco, *Intermetallics* **2019**, *108*, 32–38.

[36] L. Truong-Phuoc, J.-M. Nhut, G. Giambastiani, C. Pham-Huu, A. Jourdan, in *Procédé de conversion du CO2 en méthane*, **2021**.

[37] M. Biset-Peiró, J. Guilera, T. Andreu, *Chem. Eng. J.* **2022**, *433*, 133638.

[38] Z. R. Ismagilov, S. V. Lazareva, N. V. Shikina, V. V. Kuznetsov, M. A. Kerzhentsev, Y. V. Ostrovsky, N. A. Rudina, V. A. Rogova, V. A. Ushakov, *Mendeleev Commun.* **2011**, *21*, 209–211.

[39] H. Qiao, Z. Wei, H. Yang, L. Zhu, X. Yan, *J. Nanomater.* **2009**, *2009*, 795928.

[40] S. Zhang, S. Gai, F. He, Y. Dai, P. Gao, L. Li, Y. Chen, P. Yang, *Nanoscale* **2014**, *6*, 7025–7032.

[41] R. Jenkins, R. L. Snyder, *Introduction to X-ray Powder Diffractometry*, John Wiley & Sons Inc., **1996**, pp. 89–91.

[42] K. Popa, O. Walter, O. Dieste Blanco, A. Guiot, D. Bouëxière, J.-Y. Colle, L. Martel, M. Naji, D. Manara, *CrystEngComm* **2018**, *20*, 4614–4622.

[43] M. Urbonavicius, S. Varnagiris, L. Pranevicius, D. Milcius, *Materials* **2020**, *13*, 1300 (1312).

[44] C. Falaise, C. Volkringer, R. Giovine, B. Prelot, M. Huvea, T. Loiseau, *Dalton Trans.* **2017**, *46*, 12010–12014.

[45] B. Liu, L. R. Liu, X. J. Liu, M. J. Liu, Y. S. Xiao, *Mater. Sci. Technol.* **2012**, *28*, 1345–1348.

[46] D. Liu, D. Li, D. Yang, *AIP Adv.* **2017**, *7*, 015028.

[47] J. Lin, I. Dahan, B. Valderrama, M. V. Manuel, *Appl. Surf. Sci.* **2014**, *301*, 475–480.

[48] M. Caporali, M. Serrano-Ruiz, F. Telesio, S. Heun, G. Nicotra, C. Spinella, M. Peruzzini, *Chem. Commun.* **2017**, *53*, 10946–10949.

[49] F. J. Berry, A. Murray, N. D. Parkyns, *Appl. Catal. A* **1993**, *100*, 131–143.

[50] K. S. W. Sing, D. H. Everett, R. A. W. Haul, L. Moscou, R. A. Pierotti, J. Rouquérol, T. Siemieniewska, *Pure Appl. Chem.* **1985**, *57*, 603-619.

[51] T. Montini, V. Gombac, A. Hameed, L. Felisari, G. Adami, P. Fornasiero, *Chem. Phys. Lett.* **2010**, *498*, 113–119.

[52] S. B. Donald, M. L. Davisson, Z. Dai, S. K. Roberts, A. J. Nelson, *J. Nucl. Mater.* **2017**, *496*, 353–361.

[53] J. A. Farmer, C. T. Campbell, *Science* **2010**, *329*, 933–936.

[54] F. Javadpour, J.-P. Nicot, *Transp. Porous Media* **2011**, *89*, 265–284.

[55] H. Singh, A. Islam, *Int. J. Heat Mass Transfer* **2018**, *121*, 463–476.

[56] I. Istadi, N. A. Saidina Amin, *J. Nat. Gas Chem.* **2004**, *13*, 23–35.

[57] S. E. Kondawar, C. R. Patil, C. V. Rode, *ACS Sustainable Chem. Eng.* **2017**, *5*, 1763–1774.

[58] C. Fukuhara, S. Ratchahat, Y. Suzuki, M. Sudoh, R. Watanabe, *Chem. Lett.* **2019**, *48*, 196–199.

[59] C. Fukuhara, A. Kamiyama, M. Itoh, N. Hirata, S. Ratchahat, M. Sudoh, R. Watanabe, *Chem. Eng. Sci.* **2019**, *219*, 115589.

[60] A. N. Subbotin, B. S. Gudkov, V. I. Yakerson, *Russ. Chem. Bull. Int. Ed.* **2000**, *49*, 1373–1379.

[61] A. N. Subbotin, I. R. Subbotina, E. Z. Golosman, *Mendeleev Commun.* **2015**, *25*, 216–218.

[62] J. Bremer, K. Sundmacher, *React. Chem. Eng.* **2019**, *4*, 1019–1037.

[63] K. S. Park, M. Son, M.-J. Park, D. H. Kim, J. H. Kim, S. H. Park, J.-H. Choi, J. W. Bae, *Appl. Catal. A* **2018**, *549*, 117–133.

[64] H. Frey, A. Beck, X. Huang, J. A. van Bokhoven, M. G. Willinger, *Science* **2022**, *376*, 982–987.

[65] L. Yu, G. Wang, G. Wan, G. Wang, S. Lin, X. Li, K. Wang, Z. Bai, Y. Xiang, *Dalton Trans.* **2016**, *45*, 13779–13786.

[66] S. Dunn, P. Roussel, C. Poile, M. Higginson, P. Kaye, T. Shaw, M. R. Gilbert, J. F. Watts, *J. Radioanal. Nucl. Chem.* **2022**, *331*, 79–88.